Chapter 6

Semi-Analytical Model for Skewed Magnet Axial Flux Machine

6.1 Introduction

The compact size, low inertia and comparatively high power density distinguish axial flux permanent magnet (AFPM) machine from other variants of PM machines. AFPM machines have been widely explored for wind power generation, electric vehicle, ship propulsion, magnetic disk drives and many more industrial as well as home appliances. Due to the ease of designing high pole AFPM machine, it is a strong candidate for low speed direct drive applications. Hence, AFPM machines based direct drive systems have also been explored significantly. Furthermore, the unique feature of adjusting the rotor inertia without affecting the machine performance encourages its application for flywheel motor-generator set as energy storage system. However, the biggest challenge of permanent machine design is cogging torque, which produces several undesirable characteristics such as torque ripples, speed ripples, vibration and noise in machine. Though in high speed drives, the effect of cogging torque is compensated by inertia, but it adversely affects machine performance in case of low speed, light load and direct machine drives.

Cogging torque analysis and reduction have been extensively investigated. Various design modifications such as magnet shifting, uneven distribution of slots, uneven width of slots/teeth, slot skewing, magnet skewing and dummy slots on stator teeth have been suggested for the cogging torque reduction in PM machines [91]- [205]. All these techniques have been addressed for radial flux machine, but most of them are equally applicable to

AFPM machine. However, because of the additional manufacturing complexity and cost, some of the reported cogging torque reduction techniques are prohibited for the mass manufacturing and machine production. Alternatively, due to the ease of manufacturing magnets of different shapes, the cogging torque reduction via magnet shaping is economical and viable solution. Hence, the authors [206] have discussed various shapes of skewed magnet for cogging torque in AFPM machine and analyzed them with FEM.

In general, the design for cogging mitigation focuses on the alteration of either varying magnetic field distribution or slot distribution and hence the machine performance in terms of magnetic field distribution, linkage flux and induced EMF also get affected. Therefore, the estimation of machine performance is essential for the modified machine. The common practice for analysis is either based on FEM or analytical method. The accuracy of FEM is higher than analytical as it account of magnetic saturation and irregular geometry. However, due to high time consumption, it is not preferable for iterative design process and optimization. Alternatively, designers mostly rely on analytical analysis for initial stage of design as it provides the performance of machine in terms of machine dimensions and its material properties.

The analytical analysis and modeling of axial flux machine is inherently three dimensional as the analysis need to incorporate the end edge effects and hence increases the complexities of analytical field solution. Several analytical analysis have been developed for the AFPM machine, which approximate the 3D machine into 2D linear topology. However, the discrepancy in the analytical and FEM results are high due to the leakage flux at the inner radius of the machine. Many research have successfully incorporated 3D field effects in the two dimensional analysis [162]- [165]. The authors in paper [163] extracted the 3D field solution of axial permanent magnet machines from its exact 2D analytical solution. They developed a radial dependence function $g(r)$ as a multiplier with the help of FEM analysis to include the edge effect. Later on, the authors discussed the method of evaluating radial dependence function $g(r)$ [163]. The experiment demonstrated in paper [163] shows the highest accuracy of solution at the mean radius of machine, but, the high discrepancy at edges (inner radius and outer radius of machine). The authors used multislice method, that is the machine is divided into several annular slices and the field solutions of each slice were added algebraically to achieve the analytical solution of an axial flux machine with semi closed slots.

In this chapter, the analytical method of analysis for AFPM machine with skewed magnets is developed. The foregoing chapter is divided into two sections viz. section one deals with the development of AFPM with skewed magnet while section two includes analytical development of triangular skewed PM machine. Both machines analysis have used the combined method of multislice approach [162], [165] and subdomain analysis. The advantage of multislice method is reduction of three dimensional problem into two dimension, while subdomain method determines magnetic field distribution in each slice analytically. The open circuit magnetic field distribution is used for cogging torque investigation. The analytically obtained field solution is validated with FEM results. Based on the analytical analysis, influence of slot shape and slot opening shape on the cogging torque is investigated comprehensively.

6.2 Analysis for Skewed Magnet Axial Flux Machine

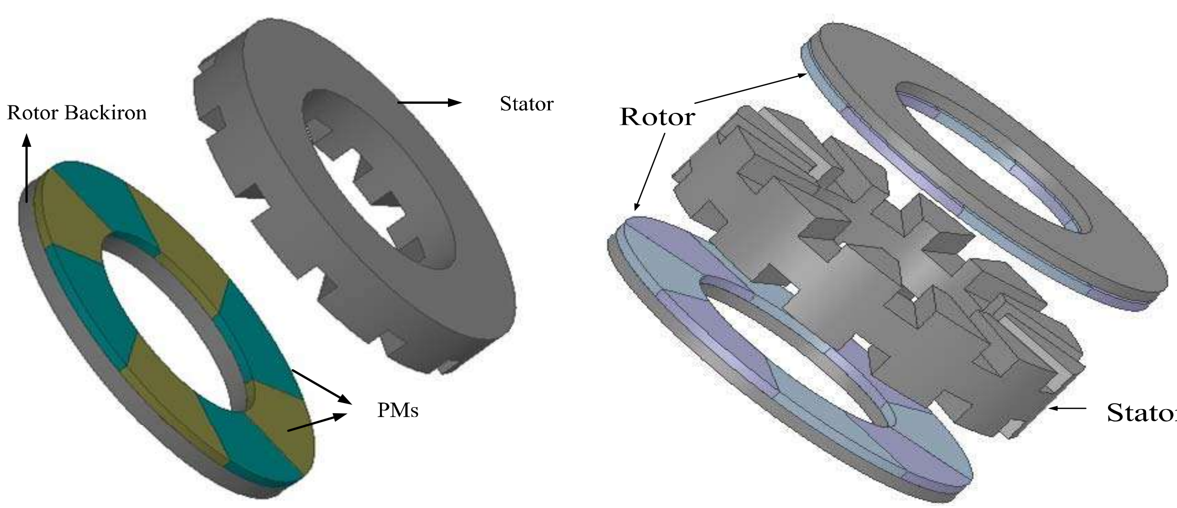

(a) Single Sided AFPM Machine (b) Double Sided AFPM Machine

Figure 6.1: Axial Flux Permanent Magnet Machine

Analytical Analysis

In this section, the analytical model for both single rotor and double rotor AFPM with skewed magnets are developed. The Figure-6.1 depicts both the variants of axial machine, while Figure-6.2 shows the difference of unskewed and skewed magnet on the rotor. In the skewed magnet AFPM machine, the location of direct axis of magnet shift

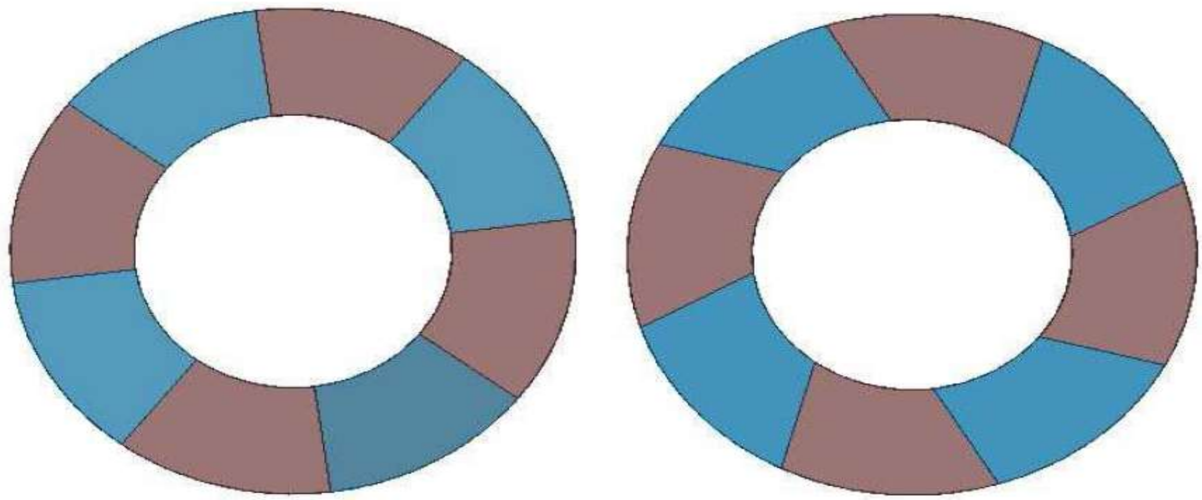

(a) Unskewed PM

(b) Skewed PM

Figure 6.2: Rotor of Axial Flux Permanent Magnet Machine

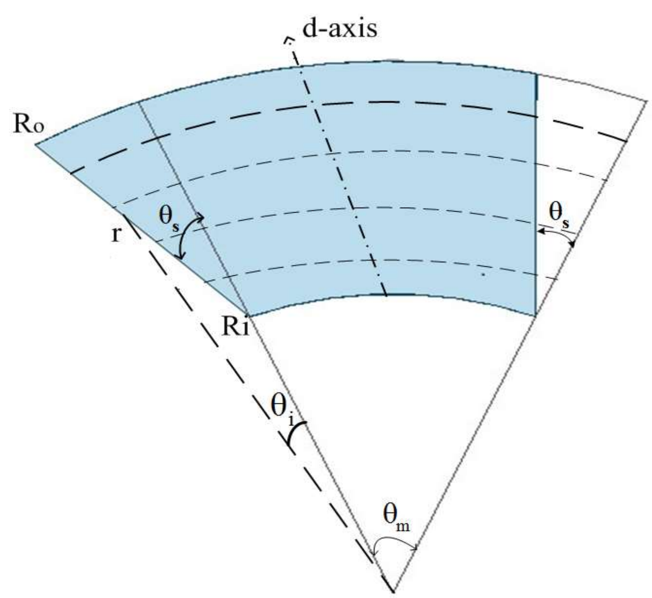

Figure 6.3: Rotor Structure with Skewed Magnet

gradually in peripheral direction, as it is being traced from inner radius to outer radius of rotor core as shown in the Figure-6.3. The machine is divided into a certain numbers of annular slices in the radial direction. The direct axis of each slice is displaced by a certain angle. The analytical model is based on the solution of Maxwell equations and it is established at the average radius of each slice. The multislice approach takes the accountability of 3D up to certain extent.

The two dimensional model for AFPM is achieved by unrolling an infinitesimally

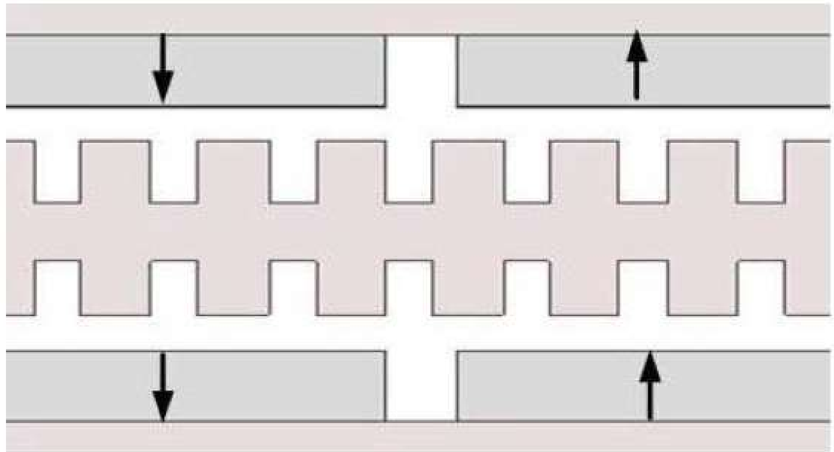

(a) Dual Rotor

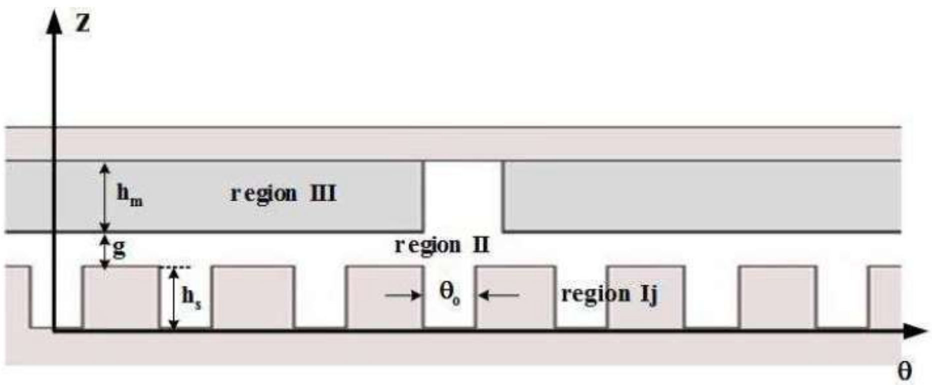

(b) Single Rotor

Figure 6.4: Unrolled Portion of Axial Permanent Magnet Machine

small thick slice at radius r. The Figure-6.4a, and Figure-6.4b show the linear equivalent model for dual sided and single sided AFPM machine respectively. The complete 3D model is comprises of infinite many slice models, whose rotor differ from each other by an rotational angle. The slice model present at an arbitrary radius r is displaced with respect to slice model at inner radius R_i by θ_i, which is defined as $\theta_i = \theta_s(r - R_i)/r$, where θ_s is skewed angle. For the analysis of dual rotor machine, due to symmetry of linear model shown in Figure-6.4a, half of the model is analyzed. With consideration of above assumptions, the simplified 2-dimensional model is as shown in the Figure-6.4b. Hence, effectively analytical modeling for single sided machine is developed and extended for dual rotor machine.

6.2.1 Analytical Prediction of No Load Magnetic Field

The magnetic field analysis for a slice located at radius r is established. The linear model of the slice is depicted in the Figure-6.4b. With the following assumptions

1. Stator is assumed to be unsaturated, and hence the relative permeability is assumed to be constant.

2. Radial magnetic flux has been ignored. However, the radial fringing is accounted by use of correction factor.

3. Magnets demagnetization curve is straight.

the machine is divided into $(Qs+2)$ regions viz. region 1j, where j is slot numbers, air-gap II, and permanent magnet region III. For the permanent magnet machines, $\overrightarrow{B}$ and $\overrightarrow{H}$ are coupled as

$$\overrightarrow{B} = \begin{cases} \mu_0 \overrightarrow{H}_I & \text{In slot region Ij} \\ \mu_0 \overrightarrow{H}_{II} & \text{In airgap region II} \\ \mu_0 \mu_r \overrightarrow{H}_{III} + \mu_0 \overrightarrow{M} & \text{In PM region III} \end{cases} \tag{6.1}$$

where **M**, μ_r and μ_0 are the remanent magnetization, relative permeability of permanent

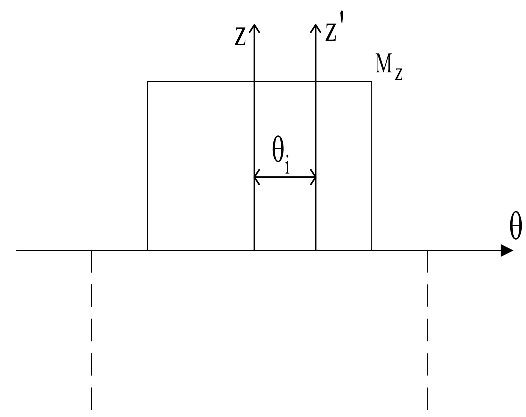

Figure 6.5: Magnetization Distribution

magnet and free space absolute permeability respectively. The remanent flux density and permeability of the permanent magnet is related as $B_{rem} = \frac{M}{\mu_o}$. The magnetization distribution pattern written in rotor frame attached to d-axis of permanent magnet at inner radius is shown in Figure-6.5 can be expanded in Fourier series as

$$\mathbf{M}_z = \sum_{n=1,2,3..}^{\infty} M_n \mathrm{cos} n\left(\theta - \theta_i - \alpha\right) \tag{6.2}$$

where α is arbitrary location of magnet from stator coordinate frame, and

$$M_n = \begin{cases} \frac{4PB_r}{\mu_o n\pi} \sin\left(\frac{n\pi\alpha_p}{p}\right) & \text{if } \ \mathrm{n} = \mathrm{jp}, \ \ \mathrm{j} = 1,3,5.... \\ 0 & \text{otherwise} \end{cases} \tag{6.3}$$

The governing equation for magnetic field has been formulated in terms of magnetic vector potential $\mathbf{A}$ defined as $\mathbf{B} = \nabla \times \mathbf{A}$.

$$\left.\begin{aligned} \mathbf{B}_z &= -\frac{\partial \mathbf{A}_r}{r\partial\theta} \\ \mathbf{B}_\theta &= \frac{\partial \mathbf{A}_r}{\partial z} \end{aligned}\right\} \tag{6.4}$$

The governing field equations in all regions, in terms of Coulomb gauge, $\nabla.\mathbf{A} = 0$, are

$$\nabla^2 \mathbf{A}_r = \begin{cases} 0; & regionIj \\ 0; & regionII \\ -\mu_0 \nabla \times M; & regionIII \end{cases} \tag{6.5}$$

Effectively, the governing equations in all regions can be rewritten in a coordinate frame attached with stator as

$$\left.\begin{aligned} \frac{1}{r^2}\frac{\partial \mathbf{A}_{Ijr}}{\partial r} + \frac{1}{r}\frac{\partial^2 \mathbf{A}_{Ijr}}{\partial \theta^2} &= 0 \\ \frac{1}{r^2}\frac{\partial \mathbf{A}_{IIr}}{\partial r} + \frac{1}{r}\frac{\partial^2 \mathbf{A}_{IIr}}{\partial \theta^2} &= 0 \\ \frac{1}{r^2}\frac{\partial \mathbf{A}_{IIIr}}{\partial r} + \frac{1}{r}\frac{\partial^2 \mathbf{A}_{IIIr}}{\partial \theta^2} &= -\frac{\mu_o}{r}\frac{\partial \mathbf{M}_z}{\partial \theta} \end{aligned}\right\} \tag{6.6}$$

The boundary conditions to be satisfied by solution of above partial differential equations are described as below:

Because of infinite permeability of stator, the boundary conditions on the field in the slot regions are

$$\mathbf{B}_{Ij\theta}(\theta, z)\big|_{z=0} = 0 \tag{6.7}$$

and,

$$\mathbf{B}_{Ijz}(\theta, z) = 0; \qquad \forall\, \theta \in \left\{-\frac{\theta_o}{2} + \frac{2\pi j}{Q_s}, \frac{\theta_o}{2} + \frac{2\pi j}{Q_s}\right\} \tag{6.8}$$

Considering the boundary conditions given in the equations (6.7), and (6.8) and applying the variable separable method, the potential in slot region is given as

$$\mathbf{A}_{Ijr} = a_0^j + \sum_k a_k^j \frac{r\theta_o}{k\pi} \cosh \frac{k\pi z}{r\theta_o} \cos \frac{k\pi\theta}{r\theta_o} \tag{6.9}$$

The other boundary conditions at interface of magnet and airgap regions are

$$\mathbf{H}_{II\theta} = \mathbf{H}_{III\theta}|_{z=(h_s+g)}; \;\; \mathbf{B}_{III\theta}(\theta, z)|_{z=(h_s+g+h_m)} = 0 \tag{6.10}$$

In view of this, the vector potential in airgap and magnet regions are given as

$$\begin{aligned} \mathbf{A}_{IIr} &= \sum_{n=1}^{\infty} \tfrac{r}{n}\left\{a_{IIn}\sinh(\tfrac{nz}{r}) + b_{IIn}\cosh(\tfrac{nz}{r})\right\}\sin n\theta \\ &- \sum_{n=1}^{\infty} \tfrac{r}{n}\left\{c_{IIn}\sinh(\tfrac{nz}{r}) + d_{IIn}\cosh(\tfrac{nz}{r})\right\}\cos n\theta \end{aligned} \tag{6.11}$$

and,

$$\begin{aligned} \mathbf{A}_{1r} &= \sum_{n=1}^{\infty} \tfrac{r}{n}\left\{a_{In}\sinh(\tfrac{nz}{r}) + b_{In}\cosh(\tfrac{nz}{r}) + G_n\right\}\sin n\theta \\ &- \sum_{n=1}^{\infty} \tfrac{r}{n}\left\{c_{In}\sinh(\tfrac{nz}{r}) + d_{In}\cosh(\tfrac{nz}{r}) + H_n\right\}\cos n\theta \end{aligned} \tag{6.12}$$

where, $G_n = \mu_o M_n \sin n(\theta_i+\alpha)$, and $H_n = \mu_o M_n \cos n(\theta_i+\alpha)$. To evaluate the coefficients involved in the vector potential expression, following boundary conditions are used

$$\mathbf{B}_{Ijz} = \mathbf{B}_{IIz}|_{z=h_s} \tag{6.13}$$

$$\mathbf{B}_{III\theta}(\theta, z)|_{z=(h_s+g+h_m)} = 0 \tag{6.14}$$

and,

$$\mathbf{H}_{II\theta}|_{z=h_s} = \begin{cases} \mathbf{H}_{Ij\theta}; \;\; \forall\,\theta \in \left[-\frac{\theta_o}{2} + \frac{2\pi j}{Q_s}, \frac{\theta_o}{2} + \frac{2\pi j}{Q_s}\right] \\ 0; \qquad \forall\,\theta \notin \left[-\frac{\varphi_o}{2} + \frac{2\pi j}{Q_s}, \frac{\varphi o}{2} + \frac{2\pi j}{Q_s}\right] \end{cases} \tag{6.15}$$

The coefficient determination is very much similar to the process described in chapter 3. The air gap magnetic field distributions are given as

$$\begin{aligned} \mathbf{B}_{IIz}(z,\theta) &= \sum_{n=1}^{\infty} \left\{a_{IIn}\sinh(\tfrac{nz}{r}) + b_{IIn}\cosh(\tfrac{nz}{r})\right\}\sin n\theta \\ &- \sum_{n=1}^{\infty} \left\{c_{IIn}\sinh(\tfrac{nz}{r}) + d_{IIn}\cosh(\tfrac{nz}{r})\right\}\cos n\theta \end{aligned} \tag{6.16}$$

and

$$\begin{aligned} \mathbf{B}_{II\theta}(z,\theta) &= \sum_{n=1}^{\infty} \left\{a_{IIn}\sinh(\tfrac{nz}{r}) + b_{IIn}\cosh(\tfrac{nz}{r})\right\}\cos n\theta \\ &+ \sum_{n=1}^{\infty} \left\{c_{IIn}\sinh(\tfrac{nz}{r}) + d_{IIn}\cosh(\tfrac{nz}{r})\right\}\sin n\theta \end{aligned} \tag{6.17}$$

6.2.2 Cogging Torque Calculation

The cogging torque is calculated by use of Maxwell stress tensor [163]

$$T = \frac{1}{\mu_o} \iint\limits_S r B_{IIz} B_{II\theta} ds \tag{6.18}$$

where, B_{IIz}, $B_{II\theta}$ are axial and tangential flux densities at magnet surface, S is the PMs surface and defined as $ds = rdrd\theta$, which is further simplified as

$$T_{cog} = \frac{1}{\mu_o} \int_0^{2\pi} \int_{r_i}^{r_o} B_{IIz} B_{II\theta} r^2 dr d\theta \tag{6.19}$$

For multislice modeling of axial flux machine, the total cogging developed in machine is calculated as algebraic summation of cogging torque produced due to each slice.

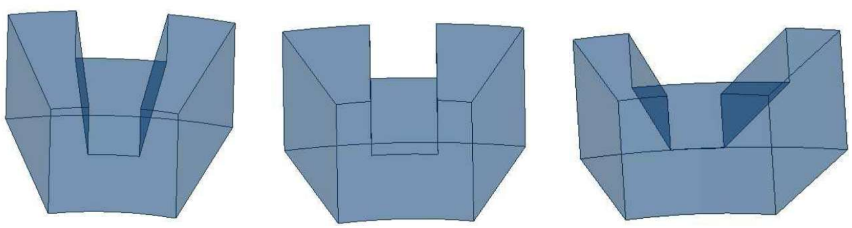

(a) Type 1 (b) Type 2 (c) Type 3

Figure 6.6: Axial Flux Permanent Machine's Slot Type a) Type 1: Trapezoidal Slot , b)Type 2: Parallel Slot and c)Type 3: Parallel Teeth

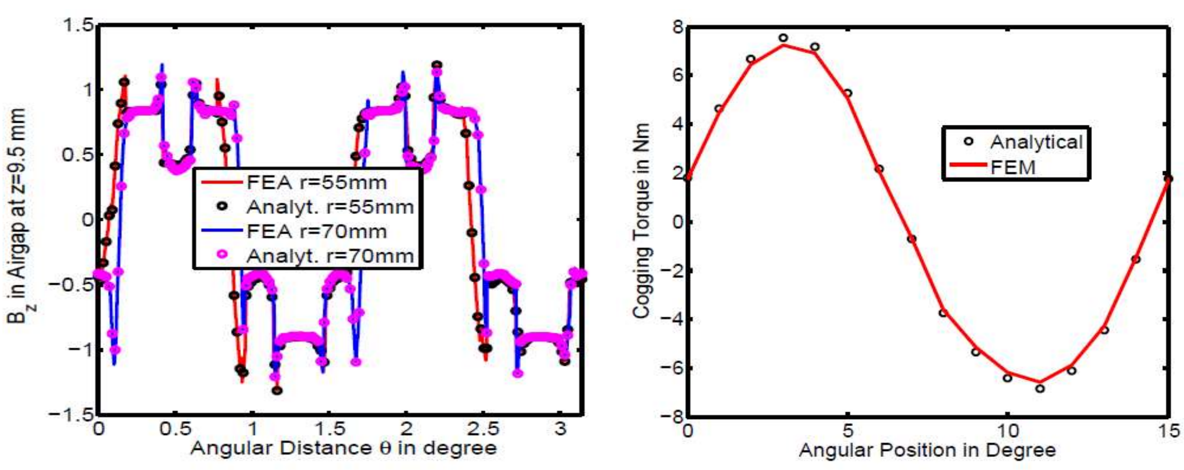

(a) Airgap Flux Density (b) Cogging Torque

Figure 6.7: Comparison of Analytical and FEM Results for Type 1:Trapezoidal Slot

Table 6.1: Dimensional Details of Skewed Magnet Axial Machine

Machine's Parameters	Values
No of poles (p)	8
No of Slots (Q_s)	12
Slot Height (h_s)	10 mm
Inner Radius (R_i)	45 mm
Outer Radius (R_o)	90 mm
Magnet Height (h_m)	4 mm
Magnet Pitch θ_m	$\pi/4$
Magnet Skewed Angle θ_s	$\pi/12$
Air gap (g)	1 mm
Slots Width at $r = R_i, \theta_o$	12^o (type1), 12^o (type2), 12^o (type3)
Slots Width at $r = R_o, \theta_o$	12^o (type1), 6.75^o (type2), 19.875^o (type3)
B_r, μ_r	1.1T,1.05

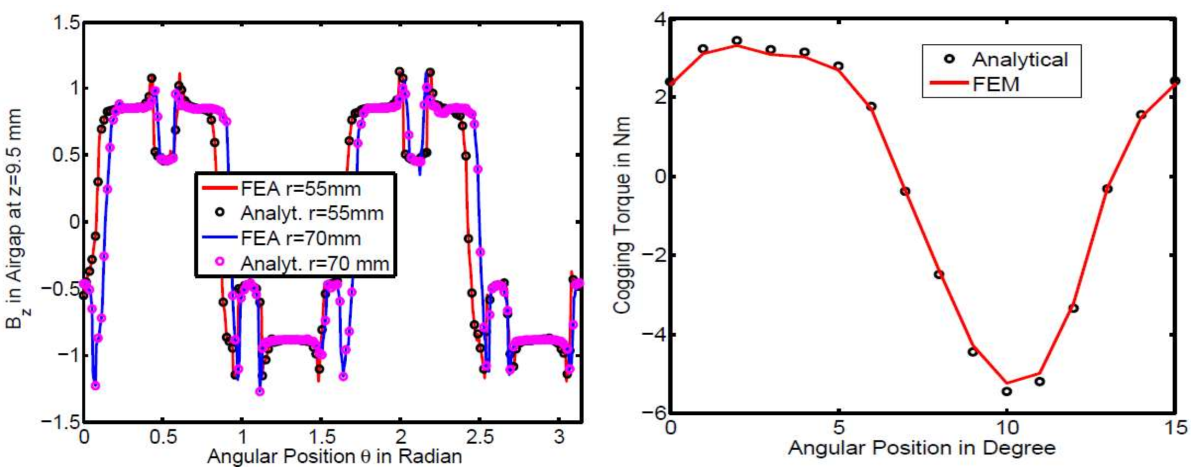

(a) Airgap Flux Density

(b) Cogging Torque

Figure 6.8: Comparison of Analytical and FEM Results for Type 2: Parallel Slot

6.2.3 Finite Element Analysis and Analytical Results Comparison

The developed analytical solution is verified with Finite Element Analysis (FEA). The FEA is obtained by use of 3D modeling in ANSYS MAXWELL 18.0 software. Three different shapes of open slots viz. type 1: trapezoidal slot , type 2: Parallel slot and

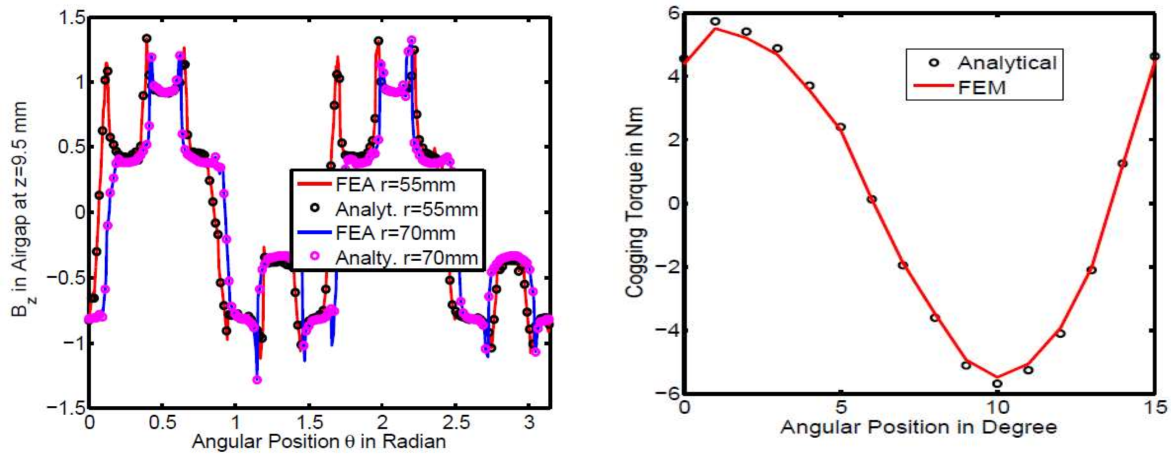

(a) Airgap Flux Density (b) Cogging Torque

Figure 6.9: Comparison of Analytical and FEM Results for Type 3: Parallel Teeth

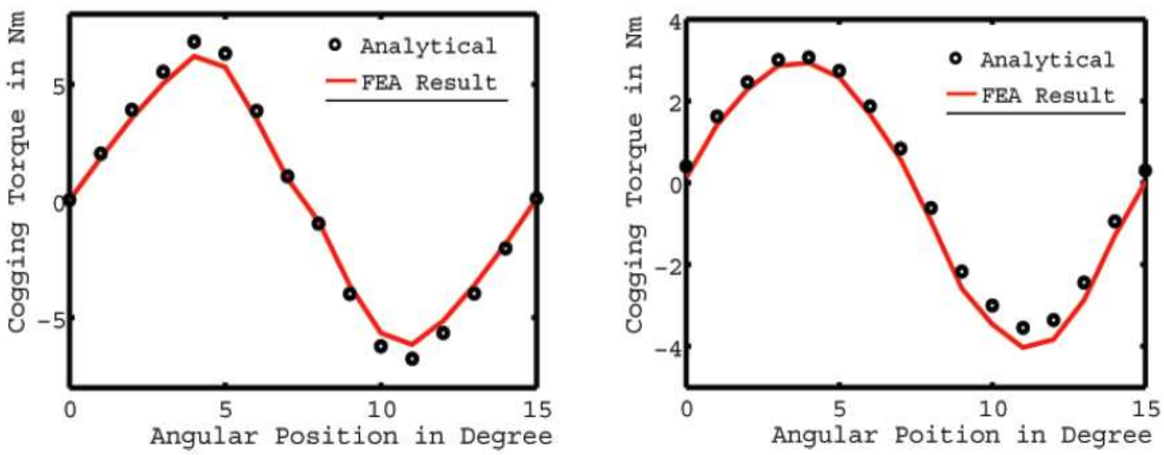

(a) Unskewed AFPM Machine (b) Skewed AFPM Machine

Figure 6.10: Cogging Torque Comparison for Type1

type3: parallel teeth shown in the Figure-6.6 are considered for no-load magnetic field and cogging torque investigation. Slots cross sectional area varies with radius with minimum area at inner radius. To maintain constant electrical loading of machine, the slot area for all slot types are kept constant. The airgap magnetic flux density distribution are obtained analytically, and compared with FEA results. For all slot shapes, the airgap flux density at two different locations i.e., (i) z = 9.5 mm and and r = 55 mm, and (ii) z = 9.5 mm and and r = 70 mm are plotted in Figures-6.7a, 6.8a and 6.9a. The shift of magnet axis along with radial distance is due to magnet skewing, and is reflected in the analytical and FEA results. For type 1 slot shape, the slot angle is 12^o at every radius, while for parallel slot, slot angle

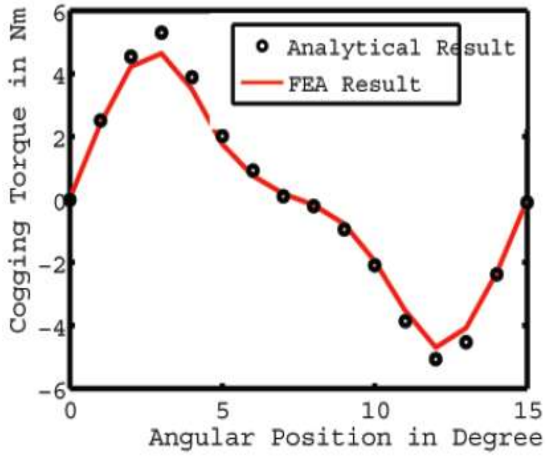

(a) Unskewed AFPM Machine

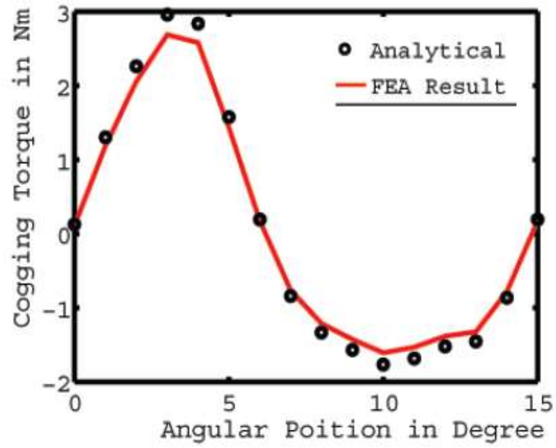

(b) Skewed AFPM Machine

Figure 6.11: Cogging Torque Comparison for type 2

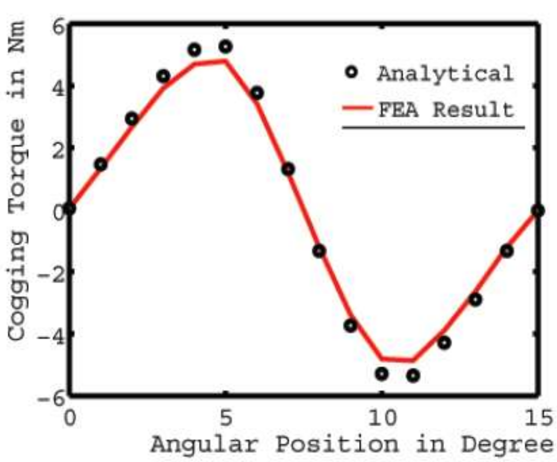

(a) Unskewed AFPM Machine

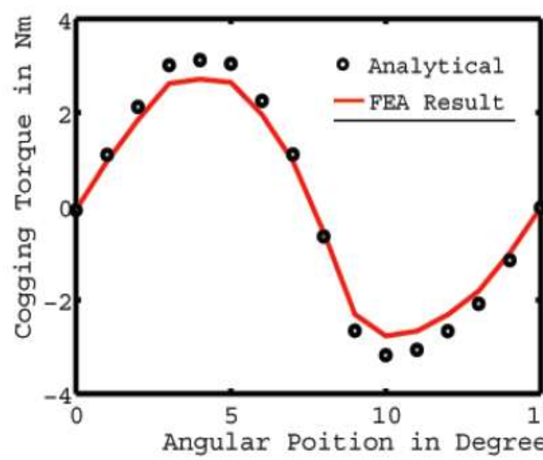

(b) Skewed AFPM Machine

Figure 6.12: Cogging Torque Comparison for Type 3

θ_o decreases with radius. Moreover, for type 3 slots, the slot angle increases with radius Figure-6.9a. In case of type 1 slot, the interaction of trapezoidal shaped skewed magnet with trapezoidal shapes slot/teeth produces highest cogging torque. Figures-6.7b,6.8b and 6.9b show the cogging torque calculated analytically and compared with FEA for all type of slot's shape. For further investigating the effect of the magnet skewing on the cogging torque, a comparative analysis of the cogging torque for skewed and unskewed magnet machine is carried out. Both analytical and FEM results are given in the figure for all three types of slots.

6.3 Analysis for Triangular Skewed Permanent Magnet Axial Flux Machine

Analytical Analysis

Flux leakage at the inner radius of the AFPM is high and it reduces the machine performance. To reduce the leakage flux and cogging torque in the machine, in this section, a triangular skewed AFPM with semiclosed slot is investigated. The method of analysis is similar to previously described.

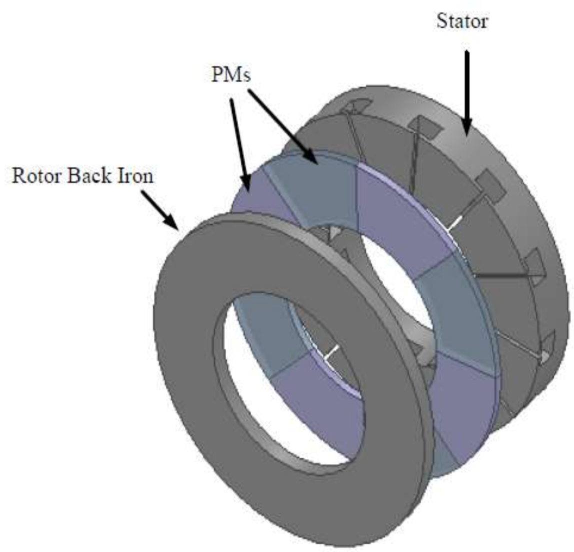

Figure 6.13: Axial Flux Permanent Magnet Machine

6.3.1 Analytical Prediction of No load Magnetic Field

In order to establish magnetic field solution, the machine is divided into certain numbers of annular slices in the radial direction, and analytical solution is obtained in two dimensional coordinate frame for each slice. The magnetic pole angle of each slice is different as shown in the Figure-6.14b. The magnet pole angle for slice located at radius r is $\theta_m + 2\theta_o$ where $\theta_o = \frac{r-R_i}{r}\delta$, and δ is defined as skewed angle. The machine geometry appears as shown in the Figure-6.15, when the annular slices are unrolled.

The magnetic field analysis is confined to four regions viz. permanent magnet region 1, air-gap 2, slot opening region 3i, and slot region 4i . The governing field equations in

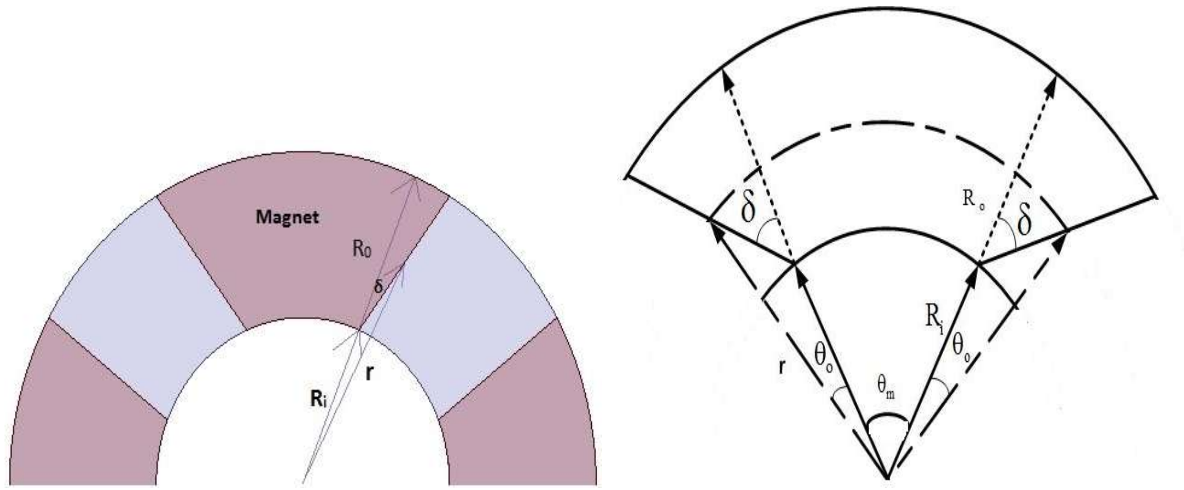

(a) (b)

Figure 6.14: Permanent Magnet Shape of Axial Flux Machine

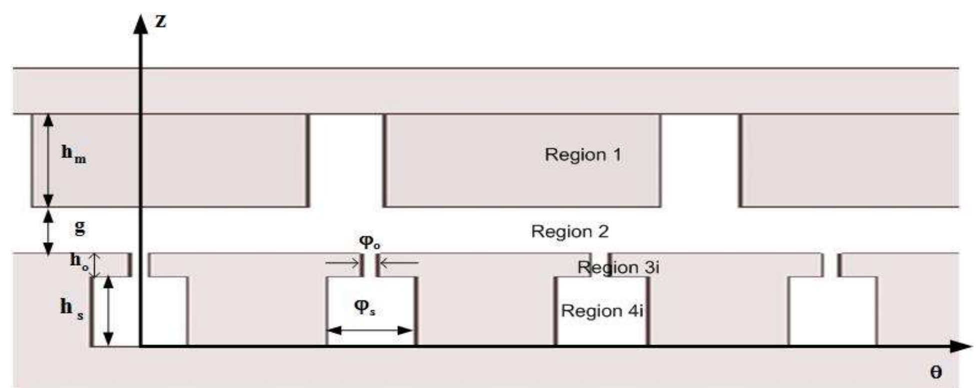

Figure 6.15: Unrolled Portion of Axial Flux Permanent Magnet Machine

all regions are

$$\frac{1}{r^2}\frac{\partial \mathbf{A}_{1r}}{\partial r}+\frac{1}{r}\frac{\partial^2 \mathbf{A}_{1r}}{\partial \theta^2}=-\frac{\mu_o}{r}\frac{\partial \mathbf{M}_z}{\partial \theta} \tag{6.20}$$

$$\frac{1}{r^2}\frac{\partial \mathbf{A}_{2r}}{\partial r}+\frac{1}{r}\frac{\partial^2 \mathbf{A}_{2r}}{\partial \theta^2}=0 \tag{6.21}$$

$$\frac{1}{r^2}\frac{\partial \mathbf{A}_{3ir}}{\partial r}+\frac{1}{r}\frac{\partial^2 \mathbf{A}_{3ir}}{\partial \theta^2}=0 \tag{6.22}$$

and,

$$\frac{1}{r^2}\frac{\partial \mathbf{A}_{4ir}}{\partial r}+\frac{1}{r}\frac{\partial^2 \mathbf{A}_{4ir}}{\partial \theta^2}=0 \tag{6.23}$$

The boundary conditions to be satisfied by solution of above partial differential equations are described as follow:

Because of the infinite permeability of the stator and rotor core, the field in the slot, slot opening and magnet regions are written as

$$\mathbf{B}_{1\theta}(\theta,z)\big|_{z=(h_s+h_o+g+h_m)}=0 \tag{6.24}$$

$$\mathbf{B}_{3iz}(\theta,z)=0; \qquad \forall\,\theta\in\left\{-\frac{\varphi_o}{2}+\frac{2\pi i}{Q_s},\frac{\varphi_o}{2}+\frac{2\pi i}{Q_s}\right\} \tag{6.25}$$

$$\mathbf{B}_{4iz}(\theta,z)=0; \qquad \forall\,\theta\in\left\{-\frac{\varphi_s}{2}+\frac{2\pi i}{Q_s},\frac{\varphi_s}{2}+\frac{2\pi i}{Q_s}\right\} \tag{6.26}$$

and,

$$\mathbf{B}_{4i\theta}(\theta,z)\big|_{z=0}=0 \tag{6.27}$$

The other boundary conditions that ensures the continuity of normal component of magnetic field density, and tangential component of field intensity are given as follows.
At the interface of magnets and airgap,

$$\mathbf{B}_{1z}=\mathbf{B}_{2z}\big|_{z=(h_s+h_o+g)}; \qquad \mathbf{H}_{1\theta}=\mathbf{H}_{2\theta}\big|_{z=(h_s+h_o+g)} \tag{6.28}$$

At the interface of airgap and slot opening,

$$\mathbf{B}_{3iz}=\mathbf{B}_{2z}\big|_{z=(h_s+h_o)} \tag{6.29}$$

and,

$$\mathbf{H}_{2\theta}\big|_{z=(h_s+h_o)}=\begin{cases}\mathbf{H}_{3i\theta}; & \forall\,\theta\in\left[-\frac{\varphi_{o.}}{2}+\frac{2\pi i}{Q_s},\frac{\varphi_o}{2}+\frac{2\pi i}{Q_s}\right]\\ 0; & \forall\,\theta\notin\left[-\frac{\varphi_o}{2}+\frac{2\pi i}{Q_s},\frac{\varphi o}{2}+\frac{2\pi i}{Q_s}\right]\end{cases} \tag{6.30}$$

At the interface of slot opening and slot,

$$\mathbf{B}_{4iz}=\mathbf{B}_{3iz}\big|_{z=h_s} \tag{6.31}$$

and,

$$\mathbf{H}_{3i\theta}\big|_{z=h_s}=\begin{cases}\mathbf{H}_{4i\theta}; & \forall\,\theta\in\left[-\frac{\varphi_o}{2}+\frac{2\pi i}{Q_s},\frac{\varphi_o}{2}+\frac{2\pi i}{Q_s}\right]\\ 0; & \forall\,\theta\notin\left[-\frac{\varphi_o}{2}+\frac{2\pi i}{Q_s},\frac{\varphi_o}{2}+\frac{2\pi i}{Q_s}\right]\end{cases} \tag{6.32}$$

Considering the boundary conditions given above and applying the variable separable method, the potential in slot region is given by

$$\mathbf{A}_{4ir}=a^i_{40}+\sum_k a^i_{4k}\frac{r\varphi_s}{k\pi}\cosh\frac{k\pi z}{r\varphi_s}\cos\frac{k\pi\theta}{r\varphi_s} \tag{6.33}$$

$$\mathbf{A}_{3ir}=a^i_{30}+\sum_k\frac{r\varphi_s}{m\pi}\left(a^i_{3m}\sinh\frac{m\pi z}{r\varphi_o}+b^i_{3m}\cosh\frac{m\pi z}{r\varphi_o}\right)\cos\frac{m\pi\theta}{r\varphi_o} \tag{6.34}$$

$$\mathbf{A}_{2r} = \sum_{n=1}^{\infty} \tfrac{r}{n}\big\{a_{2n}\sinh(\tfrac{nz}{r}) + b_{2n}\cosh(\tfrac{nz}{r})\big\}\sin n\theta \\ - \sum_{n=1}^{\infty} \tfrac{r}{n}\big\{c_{2n}\sinh(\tfrac{nz}{r}) + d_{2n}\cosh(\tfrac{nz}{r})\big\}\cos n\theta \tag{6.35}$$

and,

$$\mathbf{A}_{1r} = \sum_{n=1}^{\infty} \tfrac{r}{n}\big\{a_{1n}\sinh(\tfrac{nz}{r}) + b_{2n}\cosh(\tfrac{nz}{r}) + G_n\big\}\sin n\theta \\ - \sum_{n=1}^{\infty} \tfrac{r}{n}\big\{c_{1n}\sinh(\tfrac{nz}{r}) + d_{1n}\cosh(\tfrac{nz}{r}) + H_n\big\}\cos n\theta \tag{6.36}$$

where, $G_n = \mu_o M_n \sin n(\theta_i + \alpha)$, and $H_n = \mu_o M_n \cos n(\theta_i + \alpha)$. The above boundary conditions are also used to evaluate the coefficients. The calculation is similar to described in chapter 3. Using equation (6.35), the air gap magnetic field distributions are determined as

$$\mathbf{B}_{2z}(z,\theta) = \sum_{n=1}^{\infty} \big\{a_{2n}\sinh(\tfrac{npz}{r}) + b_{2n}\cosh(\tfrac{npz}{r})\big\}\sin np\theta \\ - \sum_{n=1}^{\infty} \big\{c_{2n}\sinh(\tfrac{npz}{r}) + d_{2n}\cosh(\tfrac{npz}{r})\big\}\cos np\theta \tag{6.37}$$

and

$$\mathbf{B}_{2\theta}(z,\theta) = \sum_{n=1}^{\infty} \big\{a_{2n}\sinh(\tfrac{npz}{r}) + b_{2n}\cosh(\tfrac{npz}{r})\big\}\cos np\theta \\ + \sum_{n=1}^{\infty} \big\{c_{2n}\sinh(\tfrac{npz}{r}) + d_{2n}\cosh(\tfrac{npz}{r})\big\}\sin np\theta \tag{6.38}$$

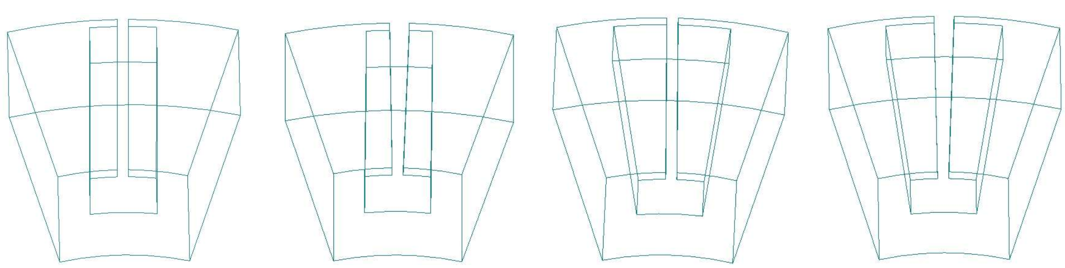

(a) (b) (c) (d)

Figure 6.16: Axial Flux Machine Slot Shape (a) Parallel Slot with Parallel Opening , (b) Parallel Slot with Trapezoidal Opening, (c) Trapezoidal Slot with Parallel Opening and (d) Trapezoidal Slot with Trapezoidal Opening

Table 6.2: Dimensional Details of Triangular Skewed PM Axial Machine

Machine's Parameters	Values
No of poles (p)	8
No of Slots (Q_s)	12
Inner Radius (R_i)	45 mm
Outer Radius (R_o)	90 mm
Magnet Height (h_m)	4 mm
Magnet Pitch at $r = R_i$	$\pi/6$
Magnet Pitch at $r = R_i$	$\pi/4$
Air gap (g)	1 mm
Slots Opening α_o	2.56^o (trapezoidal), 2 mm (Parallel)
Slots Width β_o	15^o (trapezoidal), 12 mm (Parallel)
B_r, μ_r	1.1T,1.05

6.3.2 Finite Element Analysis and Analytical Results Comparison

The obtained analytical solution is verified with Finite Element Analysis (FEA). The FEA is done with 3D modeling in Ansys Maxwell software as shown in Figure-F.5. Four different shapes of slots viz., parallel slot with parallel opening, parallel slot with trapezoidal opening, trapezoidal slot with parallel opening and trapezoidal slot with trapezoidal opening as shown in Figure-6.16 are used for cogging torque investigation. Slot's cross sectional area varies with radius with minimum area at inner radius. To maintain constant electrical loading of machine, the slot area for all variants of slot types are kept constant. The dimensional details of the AFPM machine under investigation is given in the Table 6.2. The airgap magnetic flux density distribution of triangular skewed magnet machines with different slots shapes are obtained analytically, and compared with FEA results. The flux density at $z = 9.5mm$, and at different radial distance at $r = 55mm$, and $r = 75mm$ are plotted in Figure-6.17. The change in magnet pole width with radial distance is reflected in the analytical as well as FEA solutions as shown in the Figure-6.17. The effects of the slots profiles are shown in the Figure-6.18. The flux distortion at slots for trapezoidal slots opening are more than parallel slot openings. Moreover, slots with

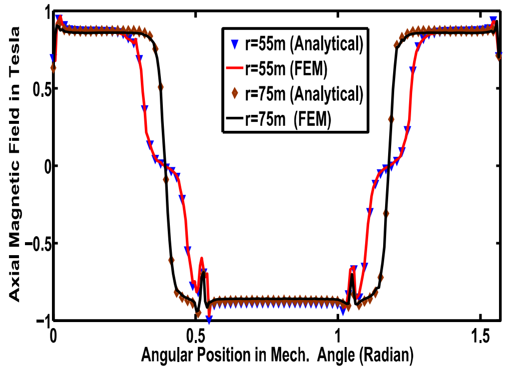

(a)

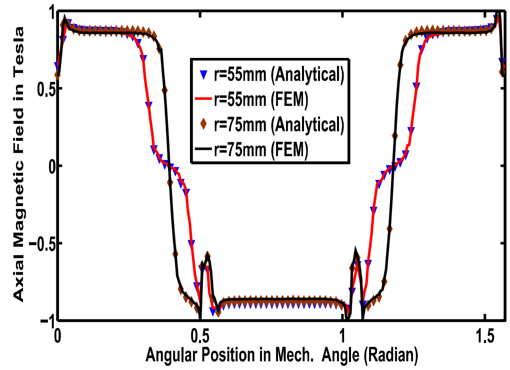

(b)

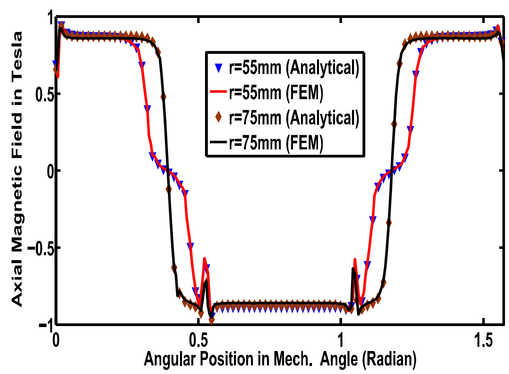

(c)

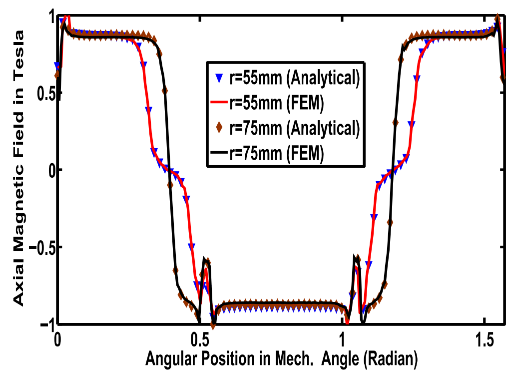

(d)

Figure 6.17: Comparison of Axial Flux Density Component at r=55mm and r=75mm (a) Parallel Slot with Parallel Opening, (b) Parallel Slot with Trapezoidal Opening, (c) Trapezoidal Slot with Parallel Opening and (d) Trapezoidal Slot with Trapezoidal Opening

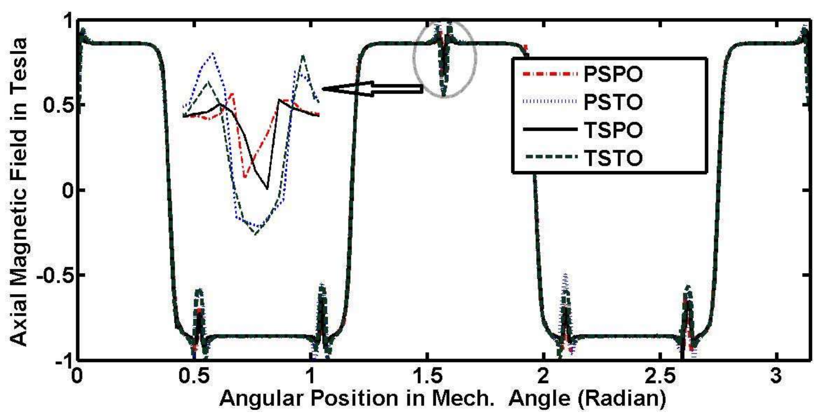

Figure 6.18: Effects of Slot Shapes on Airgap Magnetic Field Density

same types of slot opening i.e. either parallel slot with parallel opening and trapezoidal slot with parallel opening, or parallel slot with trapezoidal opening and trapezoidal slot

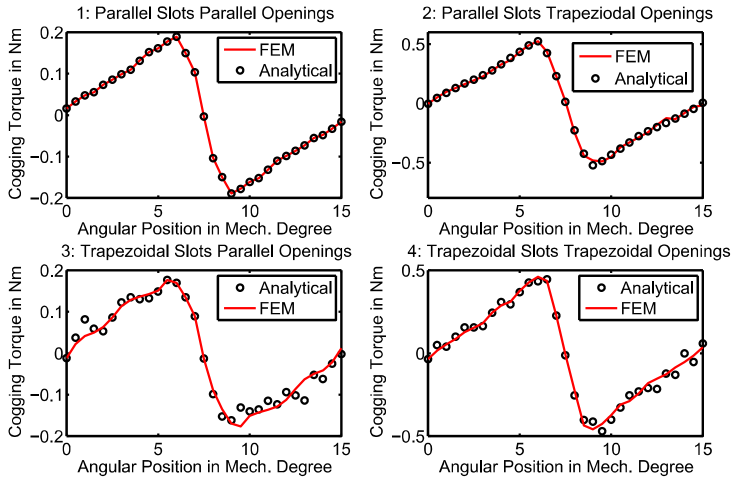

Figure 6.19: Comparison of Analytical and FEM Cogging Torque

with trapezoidal opening have same effect on field distortion, and hence it is expected that cogging torque produced by different slot shape having same kind of slot opening will produce similar cogging torque, while for different slot opening the cogging torque will be entirely different in magnitude. For multislice modeling of axial flux machine, the total cogging torque developed in machine is calculated as algebraic summation of cogging torque produced due to each slice. The analytical method adopted for the calculation is described in the section (6.2.2). The comparative plots of analytical and FEM solution for cogging torque are plotted in the Figure-6.19. The cogging torque in case of trapezoidal slot with parallel slot opening is least, but comparable to parallel slot with parallel slot opening. However, the highest cogging torque is present in parallel slot with trapezoidal slot opening. It shows the dominating influence of slot opening over slot types viz., trapezoidal slot or parallel slot, on magnetic field distortion and hence cogging torque of permanent magnet machine. Comparison of either subplots 1 and 3 or subplots 2 and 4 of Figure-6.19, shows influence of slot types on cogging torque and demonstrate the high contribution of cogging torque due to parallel slot compared to trapezoidal slot width.

6.4 Conclusion

Analytical model for skewed magnet/triangular skewed magnet axial flux machine for the magnetic field calculation has been derived. The analysis has been validated by finite element method calculations. Due to magnet skewing, the direct axis of magnet shifts in the direction of magnet skewing. A close agreement between the results obtained by these two methods have been obtained. Therefore, there is no need to apply either time consuming 3D-FEA or complex 3D analytical solution. In first section of study, three different open slots shapes are analyzed analytically and compared with FEA. The cogging torque is calculated for all and it is found that the cogging of trapezoidal slot is highest, while it is lowest for parallel teeth. While in the second section of this chapter, stator with different shapes of semi-closed slots are investigated to analyse the influence of slot , and slot opening on the cogging torque. It is found that the magnetic field distortion due to slot opening variation is more as compared to slot shape variation. Moreover, the cogging torque mainly depends on slot opening shape rather than slot shape. The skewing effects of the magnet is accounted analytically using combined approach of the multi-slice and subdomain methods. The same method could be used for analysis of a class of axial permanent magnet machine with different shapes of magnet, and stator slot variation.